Solid-State Electronics Vol. 29, No. 6, pp. 667–676, 1986
Printed in Great Britain

0038-1101/86 \$3.00 + 0.00
Pergamon Journals Ltd

EXPERIMENTAL AND THEORETICAL EVALUATION OF BORON DIFFUSED HIGH–LOW JUNCTIONS FOR BSF SOLAR CELLS

R. Girisch[†], R. P. Mertens and R. Van Overstraeten
ESAT Laboratory, Katholieke Universiteit Leuven,
Kardinaal Mercierlaan 94, 3030 Heverlee, Belgium

(*Received* 12 *March* 1985; *in revised form* 27 *September* 1985)

Abstract—An evaluation of boron diffused pp^+ high–low junctions for BSF purposes, modelled in terms of an effective recombination velocity S_{pp^+}, is presented. S_{pp^+} values are determined experimentally for three typical pp^+ high–low junctions by means of performance analysis of grating MIS solar cells with a non-inverting antireflection coating; this type of cell is very sensitive to the minority carrier reflecting capability of the back surface field, due to the two-dimensional collection mechanism. The measured S_{pp^+} values are related to the physical structure of the high–low junctions using a general mathematical formulation. It is shown that, by including as much relevant data as are now known concerning the profile of electrically active impurities N_A, Auger and SRH recombination and dopant and field dependent diffusivities, and by employing the Slotboom and de Graaff bandgap-narrowing model (degeneracy included), a good agreement is obtained between the measured S_{pp^+} values and the theoretical values. It is also established that Auger recombination has a major impact on the minority carrier reflecting capability of the high–low junctions.

1. INTRODUCTION

The incorporation of a minority carrier reflecting back surface field (BSF) can substantially improve the performance of solar cells on high resistivity substrates [1, 2]. Such cells exhibit enhanced short circuit currents and considerably higher open circuit voltages. Usually minority carrier reflecting back surface regions have been obtained by means of a high–low junction [1–4]. Alternatively a negative barrier MIS contact [5–7] or an induced accumulation layer at the back surface of the cell [11] can be used.

To clarify the improved behavior of these devices various cell analyses have been undertaken in the past decade. Analytical descriptions, in which the presence of a BSF was modelled in terms of an effective recombination velocity at the back surface S_{eff}, have been presented by Godlewski *et al.* [9], Fossum and co-workers [10], Neugroschel [8, 11] and McPartland and Sabnis [12]. Besides these models several other analytical investigations have been performed. In an early study Fossum [13] explains the device physics of the n^+pp^+ BSF cell resorting to the classical Moll–Ross analysis of minority carrier injection across an emitter–base junction [14]. The increase in the open circuit voltage was related to the increase in the integrated base doping in conjunction with the degradation of the minority carrier diffusivity in the highly doped region. Mertens and co-workers [15] and Chuang [16], who have calculated both analytically and numerically the current–voltage characteristics of n^+pp^+ diodes in dark conditions, characterized the highly doped p^+ region by a saturation current density J_{sn}. This approach is essentially equivalent to that of using a generalized effective recombination velocity, as will be formulated below.

Computer aided numerical analyses of BSF solar cells, in which the continuity equations for holes and electrons and the Poisson equation are solved simultaneously in one dimension, have been presented by Dunbar and Hauser [17, 3], and Fossum [18]. The advantages of an exact numerical approach are that available empirical information on mobility, lifetime and bandgap narrowing as a function of dopant concentration can be included and that any desired profile for the heavily doped regions can be used, which results in solutions free of limiting approximations. Obviously the minority carrier reflecting effect of a high–low junction is rigorously treated.

The effective recombination velocity S_{eff} remains, however, a valuable concept, particularly when S_{eff} is related to the physical structure of the high–low junction. To establish this relationship the carrier transport across high–low junctions has been investigated by a number of workers. The minority carrier reflecting properties of *abrupt high–low junctions* have received much attention for solar cell application [19–21]. Abrupt-junction models are valuable for modelling of e.g. Al-alloyed high–low junctions [1, 22]. However, they cannot be used for accurate modelling of diffused high–low junctions. A theoretical model, which can be applied to an *arbitrary doping profile* and which includes doping dependent carrier mobilities and lifetime as well as bandgap narrowing, has been presented by Del Alamo *et al.* [23]. Also a few experimental S_{eff} values have been published concerning diffused high–low junctions utilized as BSF in solar cells. These values have been determined either by the decomposition of measured current–voltage characteristics [10] of a p^+nn^+ cell [4, 24] or by base-width-modulation and small-signal admittance techniques [11]. However, no detailed comparison has been pursued between S_{eff} values determined by means of electrical measurements

---

[†] Present address: Philips Elcoma, Gerstweg 2, 6534 AE Nijmegen, The Netherlands.

(e.g. solar cell analysis) and S_{eff} values calculated from the impurity profile and the knowledge of carrier transport in heavily doped silicon.

The purposes of this paper are:

1) To determine S_{pp^+} values, from detailed solar cell analysis, for three typical boron-diffused high–low junctions (Section 2);

2) to calculate S_{pp^+} values from the physical structure using the general approach by Del Alamo *et al.* [23] (Section 3),

3) to compare both values and to discuss them in view of the current understanding of carrier transport in heavily doped silicon and current knowledge of physical parameters (Section 4).

2. PART 1: DETERMINATION OF S_{pp^+} VALUES FROM SOLAR CELL ANALYSIS

2.1 *Cell type under study*

As a vehicle grating MIS cells with a non-inverting antireflection coating have been used [25]. This type of cell is very suitable for the determination of S_{pp^+} values of pp^+ high–low junctions for two reasons. 1) These cells are extremely sensitive to the minority carrier reflecting capability of the BSF [25, 26] and 2) the MIS junction at the front of the cell is realized (by means of a low temperature process) after BSF formation; this guarantees that the front junction is independent of pp^+ junction formation and equal for all cells under study.

Recently we have reported on a numerical model for this type of cell [26]. Using this numerical model the experimental solar cell data are interpreted in order to determine the S_{pp^+} values. For a better understanding of this paper we shall give a short description of the model.

2.2 *Two-dimensional numerical model for grating MIS solar cells with a non-inverting antireflection coating*

Figure 1(a) and (b) display the grating cell geometry (p-type silicon). Due to the absence of charge in the antireflection coating the silicon surface layer between the MIS fingers is essentially field free. Consequently both the minority and majority carrier flows are strongly two-dimensional throughout the cell.

An exact solution to the carrier flows requires the simultaneous solution of the steady-state continuity equations for electrons and holes

$$\frac{1}{q}\nabla \cdot \vec{J}_n = -G + R \qquad (1)$$

$$\frac{1}{q}\nabla \cdot \vec{J}_p = G - R \qquad (2)$$

and the Poisson equation for the electrical potential ψ. For a better tractability of the problem we have introduced the following assumptions: 1) the MIS junction is an ideal minority carrier junction (i.e. $J_p = 0$ at the MIS interface and $\phi_m = \phi_n^{MIS}$, where ϕ_m and ϕ_n^{MIS} are the metal Fermi level and semiconductor electron quasi-Fermi level, respectively), 2) the width of the depletion layer under the MIS contact may be neglected compared to the other dimensions of interest, and 3) the effect of

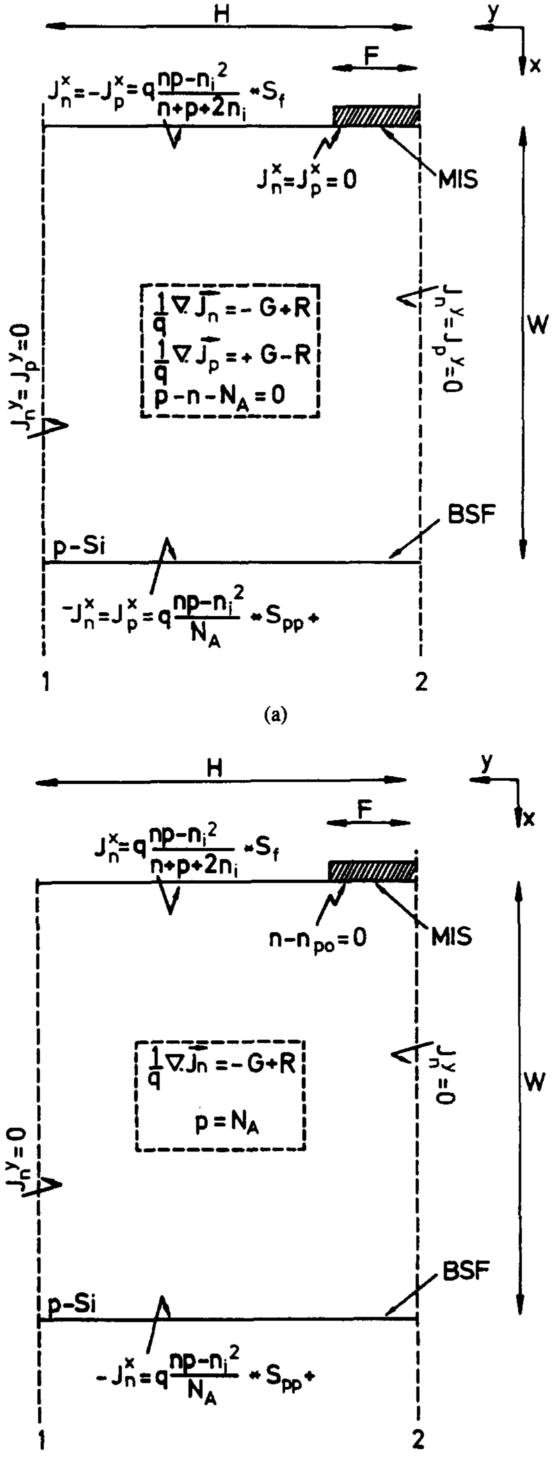

(a)

(b)

Fig. 1. (a) Unit segment of the grating MIS-NIL solar cell. Inset: basic equations solved for open circuit operation. (b) Unit segment of the grating MIS-NIL solar cell. Inset: basic equations solved for short circuit operation.

a back surface field may be modelled by an effective recombination velocity S_{pp^+} at the high–low junction (see Section 3.1). As a result of assumptions 2) and 3) only that part of the cell remains in which essentially electrical neutrality prevails. With the approximation 4) of exact electrical neutrality we can achieve approximate solutions to the electron and hole flows by the simultaneous solution of the continuity equations (1) and (2) and the charge neutrality condition

$$p - n - N_A = 0. \tag{3}$$

Open circuit voltage (V_{oc}) calculations have been performed by solving iteratively eqns (1), (2) and (3) under the appropriate boundary conditions [as shown in Fig. 1(a)]; the V_{oc} is set equal to $\phi_p^{\mathrm{BSF}} - \phi_n^{\mathrm{MIS}}$, where ϕ_p^{BSF} is the hole quasi-Fermi level at the edge of the BSF region and ϕ_n^{MIS} is again the electron quasi-Fermi level under the MIS contact.

Short circuit current (J_{sc}) calculations at AM1 illumination indicated that low level injection conditions prevail everywhere in cells with bulk dopant concentrations $N_A \geqq 10^{15}$ cm^{-3}. Therefore, short circuit current calculations only required the solution of the continuity equation (1) for electrons under the appropriate boundary conditions [as shown in Fig. 1(b)].

With this model we have investigated grating MIS-NIL cell performance as a function of cell geometry, front surface recombination velocity S_f, effective recombination velocity S_{pp^+}, and bulk lifetime τ (we have assumed equal lifetimes for electrons and holes, i.e. $\tau_n = \tau_p = \tau$). An in-depth analysis has been presented of the short circuit current (J_{sc}) dependence on half finger distance H. It has been found [26] that curve fitting of experimental $J_{sc} - H$ data of cells on BSF substrates can yield approximate values for the bulk lifetime τ, and the sum of the front surface recombination velocity S_f and the effective recombination velocity S_{pp^+}. Subsequent analyses of BSF cells on substrates with *various* high–low junctions (this paper, Section 2.4) have made us conclude S_f to be much smaller than S_{pp^+} for our BSF cells on relatively high resistivity substrates. Therefore, analyses of MIS-NIL cells on pp^+ substrates have enabled us to evaluate the recombination currents in the base and in the highly doped p^+ region and to determine approximate values for the bulk lifetime τ and the effective recombination velocity S_{pp^+} of typical pp^+ high–low junctions.

2.3 *Solar cell data analysis*

Emphasis will be placed here on the analysis of experimental $J_{sc} - H$ data, in conjunction with experimental V_{oc} data; three types of cells on different BSF substrates will be analyzed. In addition, some BSF cells with various cell thicknesses will be considered. Consistent sets of parameter values for τ and (the sum of) S_{pp^+} and S_f have been pursued. To find such a set for a particular type of cells we worked along the following lines: 1) from V_{oc} considerations a minimum value for the lifetime $\tau_{\min}$ was determined (i.e. assuming negligible recombination at the BSF and at the front); 2) for a number of values $\tau > \tau_{\min}$ corresponding values of $S_f + S_{pp^+}$ were found to account for the decrease of J_{sc} at large finger distance; 3) finally we selected the set ($\tau, S_f + S_{pp^+}$) which was considered to be optimum for both $J_{sc} - H$ data (over the whole range of H) and experimental V_{oc} data; "optimum for $J_{sc} - H$ data" was defined in the sense that the experimental and numerical J_{sc} dependence on H were similar. Generally the best fit resulted in numerical J_{sc} values somewhat lower than the experimental data (~2%). The numerical V_{oc} values tended to be slightly higher than the measured values ($\leqq$1%).

Data collection and data handling have been outlined before [26].

2.4 *Cells on different BSF substrates; equal thickness*

BSF substrates have been fabricated starting from Wacker ⟨100⟩ *p*-type silicon with resistivities of 15 Ωcm and 5 Ωcm. The pp^+ high–low junction was formed during a 1000°C drive-in cycle in nitrogen ambient using a boron doped oxide glass source. Table 1 contains the data on starting material and BSF technology. On these 3 types of substrates standard grating MIS-NIL solar cells have been fabricated; MIS cell technology has been outlined before [26]. For the sake of completeness we report that the total cell area and half finger width were 1 × 1 cm^2 and 6 μm, respectively.

In Table 2 the optimum values for τ and the sum of S_f and S_{pp^+} are given for each cell type (columns 3 and 4). It should be recalled that for each cell type individually only the *sum* of the front surface recombination velocity S_f and the effective recombination velocity S_{pp^+} can be determined [26]. However, in view of the data on substrate material and BSF technology (Table 1) the following considerations [23] have to be made: (1) the S_{pp^+} value of #1 cannot exceed twice the S_{pp^+} value of #2, and (2) the S_{pp^+} value of #3 should be about three times the S_{pp^+} value of #2. These considerations have enabled us to safely put an upper limit of 15 cm · s^{-1} for the surface recombination velocity S_f. The resulting S_{pp^+} values are given in column 6 of Table 2. In columns 7 and 8 the experimental V_{oc} values are compared with the numerical values (AM1, 27°C). The numerically generated $J_{sc} - H$ curves with the corresponding experimental data have been drawn in Figs. 2–4. Most experimental J_{sc} values are somewhat higher than the theoretical ones. No full explanation has been found for this discrepancy. Part of the discrepancy will be

Table 1. Data on starting material and BSF technology (drive-in temp.: 1000°C)

#	ρ Ωcm	N_A cm^{-3}	crystal growth	wafer thickness, μm	drive-in time, min	$R_{\square p^+}$ Ω/□
1	15	1×10^{15}	FZ	280 ± 15	30	22
2	15	1×10^{15}	FZ	280 ± 15	120	13
3	5	3×10^{15}	FZ	330 ± 20	120	12

Table 2. Optimum parameter values for numerical calculations; in columns 7 and 8 the numerical and experimental V_{oc} values are compared

#	N_A cm^{-3}	τ μs	$S_f + S_{pp^+}$ cm · s^{-1}	S_f cm · s^{-1}	S_{pp^+} cm · s^{-1}	V_{oc}^{num} mV	V_{oc}^{exp} mV	Fig.
1	1×10^{15}	612	80	0–15	65–80	604	597 ± 2	2
2	1×10^{15}	612	45	0–15	30–45	618	611 ± 2	3
3	3×10^{15}	388	130	0–15	115–130	611	611 ± 2	4

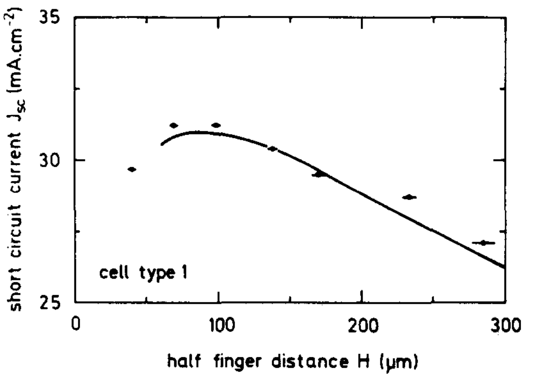

Fig. 2. Experimental J_{sc} − H data of cell type 1 (closed circles) and the numerically generated J_{sc} − H curve (solid line) for τ = 612 μs, S_{pp^+} = 70 cm · s^{-1} and S_f = 10 cm · s^{-1}.

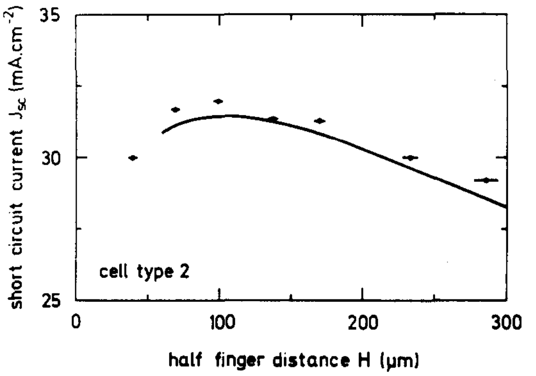

Fig. 3. Experimental J_{sc} − H data of cell type 2 (closed circles) and the numerically generated J_{sc} − H curve (solid line) for τ = 612 μs, S_{pp^+} = 35 cm · s^{-1} and S_f = 10 cm · s^{-1}.

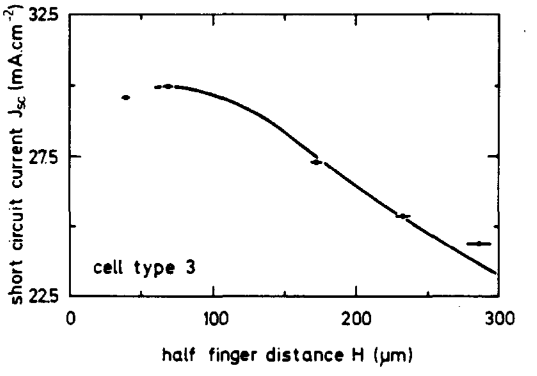

Fig. 4. Experimental J_{sc} − H data of cell type 3 (closed circles) and the numerically generated J_{sc} − H curve (solid line) for τ = 388 μs, S_{pp^+} = 120 cm · s^{-1} and S_f = 10 cm · s^{-1}.

caused by partial reflection of long wavelength light at the non-alloyed Al/Si back contact [27]. Using these data a maximum J_{sc} enhancement of 1.5% has been calculated for a typical cell configuration under study.

2.5 *Cells with various thicknesses*

A further check on the consistency of the determined τ, S_f and S_{pp^+} values was made by considering cells on substrates with various thicknesses. Both 1 × 1 cm^2 and 2 × 2 cm^2 total area cells have been analyzed with half finger distance around 120 μm. Starting material resistivity and BSF technology are similar to those of #2 in Table 1; the sheet resistance of the p^+ layer was typically 15Ω/□. In Fig. 5 the numerical J_{sc} and V_{oc} values vs cell thickness W have been displayed (S_f = 10 cm · s^{-1}, S_{pp^+} = 35 cm · s^{-1} and τ = 612 μs) together with the experimental data (AM1, 27°C). The J_{sc} data show a dependence on W similar to the numerical calculations,

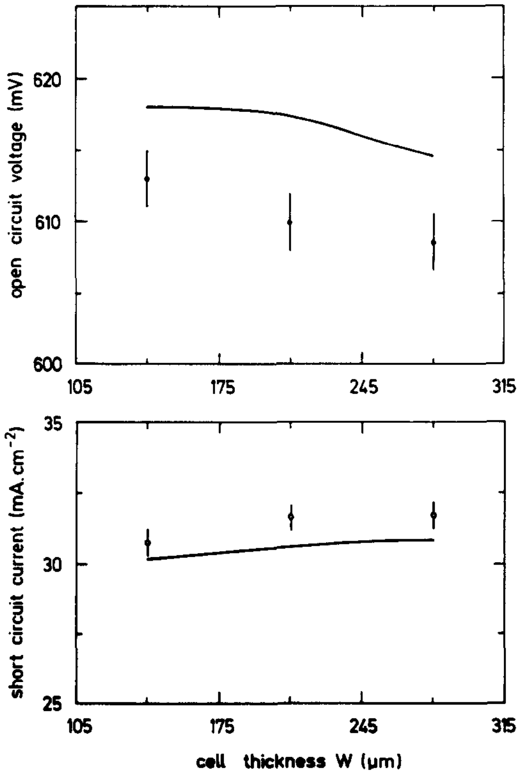

Fig. 5. Numerical J_{sc} values (bottom) and V_{oc} values (top) vs cell thickness W (τ = 612 μs, S_{pp^+} = 35 cm · s^{-1} and S_f = 10 cm · s^{-1}) together with the experimental data of cell type 2 (AM1, 27 °C).

apart from a difference in absolute value as discussed before. The experimental V_{oc} data show a small tendency to increase with decreasing cell thickness W, which was also found numerically. The experimental V_{oc} data are, however, about 1% lower than the numerical values. Further attempts to improve the fit curves did not yield consistent results. Using shorter bulk lifetimes τ (e.g. 350 μs) improved the fit for V_{oc}, but yielded poor results for J_{sc} vs H. The use of shorter lifetimes in combination with slightly lower S_{pp^+} values were also unsuccessful.

3. PART 2: S_{pp^+} CALCULATIONS FROM $N_A(x)$, ΔEg, D_n AND τ_n

3.1 *General formulation of the effective recombination velocity S_{eff}*

Here we shall address the general definition of S_{eff} and the model applied to formulate S_{eff} in terms of the dopant concentration profile, bandgap narrowing, minority carrier diffusivity and minority carrier lifetime; we shall consider the pp^+ high–low junction.

Most authors define the effective recombination velocity S_{pp^+} by [9, 23, 28]

$$-\frac{1}{q}J_n = n' \times S_{pp^+} \tag{4}$$

where J_n and n' are the electron current density and the excess electron density, respectively, at the high–low junction. As a consequence of this definition the value of S_{pp^+} is only a constant as long as the base remains in low injection, but increases linearly with carrier density n when the base reaches high injection [28, 29]. Obviously the total recombination current, injected into the p^+ region, still obeys the exponential relationship

$$-J_n = J_{sn}\{\exp(\Delta\Phi/V_T) - 1\} \tag{5}$$

where $\Delta\Phi$ represents the quasi-Fermi level separation at the high–low junction. Therefore we introduce a better definition of S_{pp^+} by

$$-\frac{1}{q}J_n = \frac{np - n_i^2}{N_A} \times S_{pp^+}. \tag{6}$$

This formulation, which guarantees that S_{pp^+} has a constant value for all injection levels in the lowly doped base, is equivalent to that by Mertens *et al.* [15] and Chuang [16], who characterized the highly doped p^+ region by a saturation current density J_{sn} [compare eqn (5)]. Obviously eqn (6) reduces to eqn (4) when the base is in low injection.

For the calculation of S_{pp^+} from doping profile $N_A(x)$, bandgap narrowing ΔEg, diffusivity D_n and lifetime τ_n we closely follow the general approach by Del Alamo *et al.* [23]. They have derived a first order nonlinear differential equation, which has to be solved to calculate S_{pp^+} for a high–low junction with an arbitrary doping profile. With the definition of the new position dependent variable

$$S = -\frac{J_n(x)}{qn'(x)} \tag{7}$$

this differential equation can be written as

$$\frac{dS}{dx} = \frac{S^2}{D_n} + \frac{S}{N_{Aeff}}\frac{dN_{Aeff}}{dx} - \frac{1}{\tau_n} \tag{8}$$

where D_n and τ_n are the position dependent electron diffusivity and lifetime, respectively, and N_{Aeff} is the effective impurity concentration [30]. In this equation it is assumed that the influence of degeneracy is also embedded in the effective intrinsic carrier density n_{ie} (or the effective dopant concentration N_{Aeff}). It has been shown that, as far as minority carrier current in low level injection is concerned, a heavily doped region with net ionized doping profile N_A behaves exactly like a nondegenerate region with dopant concentration N_{Aeff} [31, 32].

The boundary condition is the recombination velocity $S(a) = S_B$ at the back contact $x = a$ (Fig. 6). A value of 3×10^6 cm · s^{-1} was used which corresponds to the thermionic recombination velocity for electrons perpendicular to the ⟨100⟩ surface. The solution of eqn (8) at $x = o^+$ gives $S(o^+)$, which is equal to $S(o^-) \equiv S_{pp^+}$ for non-abrupt impurity profiles $N_A(x)$. In Appendix 1 we show how an iterative solution procedure of eqn (8) can be avoided.

In the derivation of S_{pp^+} low disturbance in the p^+ region is assumed implicitly. It may be argued that this condition does not hold near the high–low boundary when the base reaches high injection. However, this is inconsequential for the S_{pp^+} value obtained with eqn (8) and used in eqn (6), because the current injected into the

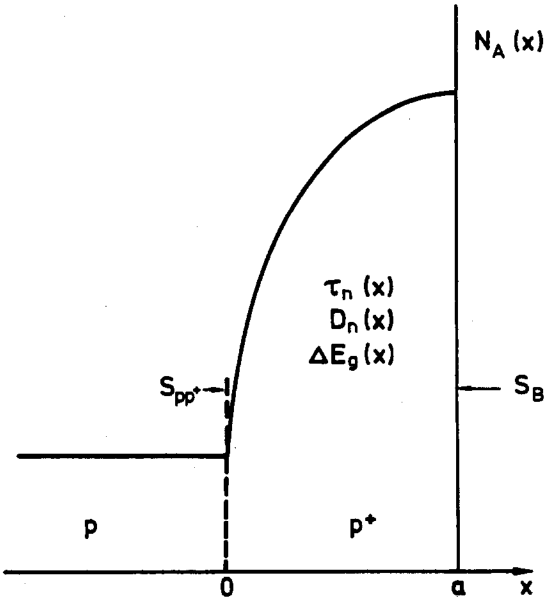

Fig. 6. Impurity profile of a pp^+ high–low junction.

p^+ region is totally determined by recombination in the heavily doped region and at the back interface (S_B) rather than by recombination in the lowly doped region near the high–low boundary. This has been verified by numerical calculations, which established that the lowly doped part of the p^+ region ($N_{Aeff} \leqq 10^{17}$ cm^{-3}) is totally transparent for minority carrier electrons.

For the concentration and field dependent minority carrier electron mobility the model presented by Selberherr [33] was used, although this model does not explicitly differentiate between majority carrier and minority carrier mobility. We shall return to this issue in the discussion (Section 4). To deduce the effective impurity concentration N_{Aeff} from the total electrically active impurity concentration N_A we used the experimentally determined formula for the bandgap narrowing ΔE_g of Slotboom and de Graaff [34], in which the effect of carrier degeneracy is embedded as well. The lifetime τ_n was considered to be determined by Auger recombination and Shockley–Read–Hall recombination, where the Kendall model [35] was applied for the SRH lifetime. The formulae will be given in Appendix 2.

3.2 *SUPREM computer simulations of boron doping profiles and comparison with measured profiles and junction depths*

For accurate modelling of carrier transport in heavily doped silicon precise knowledge of the doping profile is required. Complementary error functions, as have been used before to simulate the doping profile [23], cannot be used without significant errors because the assumption of a constant (dopant) diffusion coefficient is invalid for high-concentration diffusion.

Spreading resistance measurements and a spherical drilling technique [36] were used to identify the doping profile and depth of the heavily doped p^+ region. For this purpose np^+ junctions have been fabricated by boron drive-in cycles as described before; n-type silicon substrates (⟨100⟩, $N_D \sim 5.5 \times 10^{14}$ cm^{-3}) were used to allow accurate junction depth determination. Drive-in times of 35 min. (batch #1) and 120 min. (batch #2) have been chosen. In Fig. 7 a typical result of a spreading resistance measurement on a sample of batch #2 is compared with the theoretical curve, generated with the process simulator program SUPREM II [37]. In the SUPREM simulations one parameter, which was not known *a priori,* was adjusted to obtain optimum agreement between computed and measured sheet resistance $R_{\square,p^+}$. The measured and simulated doping profiles are similar as regards the overall shape; it should be noticed that the boron distribution is even more convex than a Gaussian distribution. In respect of the junction depth the agreement between the experimentally determined value and the theoretical one is also satisfactory (the discrepancy is about ten percent). However, the experimental concentration data at high doping levels are considerably lower than the values obtained with SUPREM. Two considerations made us conclude that the experimental concentrations are underestimated here. In the first place, the sheet resistance $R_{\square,p^+}$ calculated from the experimental data equals 20.0 Ω/□, a result which is inconsistent with the experimental value of 11.8 Ω/□, measured directly with the four-point probe method. Secondly, the boron concentration near the surface is expected to be determined by the boron solubility in Si at 1000°C (about 1.3×10^{20} cm^{-3}), because of the high dopant concentration in the oxide glass source. The inconsistent experimental results were found to be caused by the data analysis program. In this program the electrical contact diameter of the probes was assumed to be independent of dopant concentration (and numerically equal to the value at $N_A = 10^{16}$ cm^{-3}). However, the electrical contact diameter has been identified as decreasing considerably with increasing dopant concentration. Therefore, the experimental concentrations in the lower range are reliable, but the concentrations at higher levels are underestimated. Unfortunately a data analysis program, in which a concentration dependent electrical contact diameter had been implemented, was not available at the time.

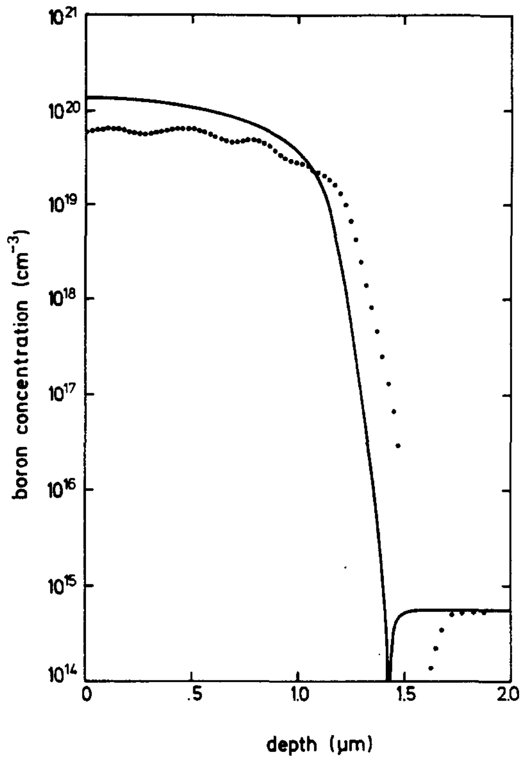

Fig. 7. Spreading resistance measurement on a sample of batch 2 (closed circles) together with the theoretical curve generated with the process simulator program SUPREM II (solid line).

In addition to spreading resistance measurements the spherical drilling technique has been applied for junction depth identification. The results for both batches are presented in Table 3 and compared to computed results. In the last column values are given, calculated according to Wang and Lo [38, eqn (19)], assuming that the concentration of (electrically active) boron at the surface is determined by the maximum solubility at 1000°C (~1.3×10^{20} cm^{-3}). The agreement between measured and calculated values is satisfactory.

Table 3. Results on junction depth determination

#	drive-in time, min.	$R_{\square, p^+}$ Ω/□	junction depth, μm experimental (drilling technique)	 SUPREM II	 analytical [38]
1	35	19.5	.9 ± .1	.81	.84
2	120	11.8	1.5 ± .1	1.41	1.38

3.3 *Results on S_{pp^+} calculations from $N_A(x)$, ΔEg, D_n and τ_n.*

For the calculations of S_{pp^+} in terms of $N_A(x)$, ΔE_g, D_n and τ_n [eqn (8)] doping profiles $N_A(x)$ have been generated with the process simulator program SUPREM II. We preferred numerically generated rather than measured profiles, because of the inaccuracy of the latter at high doping levels and also from numerical considerations. In Table 4 the results have been summarized for the pp^+ high–low junctions under study. Columns 3–5 contain information on the numerically generated profiles, column 6 the S_{pp^+} values for a transparent p^+ layer, column 7 the S_{pp^+} values neglecting SRH recombination and column 8 the S_{pp^+} values taking into account Auger and SRH recombination; the values in question for τ_o, N_{oA} and C_{ehh} are given in columns 7 and 8. In the last column the S_{pp^+} values, which had been determined from solar cell analysis, are presented. The results will be discussed in the next paragraph.

4. DISCUSSION

First we address the accuracy of the S_{pp^+} determination by means of MIS-NIL solar cell analysis. Additional consideration of the data of #3 ($N_A = 3 \times 10^{15}$ cm^{-3}) showed that J_{sc} curve fits similar to those in Fig. 5 could be obtained while varying the S_{pp^+} value with 12% provided that a higher (lower) S_{pp^+} value was compensated for by a higher (lower) τ value of 20%. The V_{oc} value also appeared to be rather insensitive to such variations in S_{pp^+} and τ. Therefore it is difficult to estimate the accuracy of the S_{pp^+} value for #3 without further experimental data (e.g. cells on wafers of various thicknesses). Further analysis of the data of #2 ($N_A = 1 \times 10^{15}$ cm^{-3}) indicated that a reduction of S_{pp^+} with 12% should be accompanied by a τ reduction of (at most) 20% to account for measured J_{sc} values. This, however, conflicted with a τ reduction of at least 33% to account for measured V_{oc} values (note that cells #2 are in medium injection around V_{oc} conditions, whereas cells #3 are virtually in low injection over the whole voltage regime). On the other hand, an increase of S_{pp^+}, accompanied by an increase of τ, resulted in V_{oc} values increasing with cell thickness, which conflicts with the experimental results mentioned in Section 3.3. Besides, lifetimes much longer than 0.6 ms seem to be rather improbable [39, 40]. Therefore the S_{pp^+} value of #2 seems to be close to the optimum.

The calculations of S_{pp^+} from doping profile $N_A(x)$, bandgap narrowing ΔE_g, diffusivity D_n and lifetime τ_n show that Auger recombination, which had not been included before [23], has a major impact on the minority carrier reflecting capability of the high–low junction (Table 4). This result agrees with those of Weaver and Nasby [41], which indicated that Auger recombination, besides bandgap narrowing, is a significant factor controlling injection currents in heavily doped silicon. For the C_{ehh} coefficient we used 1×10^{-31} cm$^6 \cdot$ s^{-1}, a value close to the experimentally determined values of Beck and Conradt [42] and Dziewior and Schmid [43], and somewhat smaller than the theoretically predicted value of Lochmann [44]. On the other hand, SRH recombination appears to be rather unimportant. The parameter values in the Kendall model were taken from Fossum [13, 18]. It may be argued that a considerable uncertainty exists concerning these values due to the sensitivity of the recombination lifetime to processing conditions. Even the validity of the Kendall model in p-type silicon may be disputed [39]. In a separate study we have performed injection-current analyses of induced-junction devices fabricated on floating-zone grown wafers with dopant concentrations ranging from 2.5×10^{15} cm^{-3} to 5×10^{17} cm^{-3} [45]. The fabrication of these devices follows closely an NMOS processing scheme including several high-temperature steps. For wafers with dopant concentration in the 10^{15} and 10^{16} decade only a lower limit for the recombination lifetime could be deduced (1×10^{-4} s), because the diffusion lengths exceeded the wafer thickness considerably. For wafers with $N_A = 5 \times 10^{17}$ cm^{-3} an effective lifetime (i.e. Auger recombination included) of 1.4×10^{-5} s was found. These results together with the high recombination lifetimes encountered in the base of the solar cells under study indicate that the employed Kendall lifetime model most likely underestimates the SRH recombination lifetimes in this p-type FZ silicon. From inspection of columns 7 and 8 (Table 4) we, therefore, conclude that SRH recombination has only a minor influence on the properties of the pp^+ junctions under study.

Table 4. Results of calculated and experimentally determined S^+_{pp} values

#	N_A cm^{-3}	N_s cm^{-3}	x_j μm	$R_{\square, p^+}$ Ω/□	S^+_{pp}, cm · s^{-1} transparent p^+	 $\tau_{SRH} \rightarrow \infty$ $C_{ehh} = 1 \times 10^{-31}$	 $\tau_o = 395$ μs $N_{oA} = 7.1 \times 10^{15}$ $C_{ehh} = 1 \times 10^{-31}$	 experimental
1	1×10^{15}	1.45×10^{20}	.75	22.1	37.7	50.7	51.3	65–80
2	1×10^{15}	1.24×10^{20}	1.36	13.2	21.1	37.5	38.3	30–45
3	3×10^{15}	1.32×10^{20}	1.36	12.1	59.8	113	116	115–130

The agreement between the theoretical S_{pp^+} values and the corresponding experimentally determined values is satisfactory (Table 4), especially for the pp^+ substrate #2 which has been analyzed most extensively. These results support evidence that the bandgap-narrowing model according to Slotboom and de Graaff [34] in conjunction with majority-carrier mobility data can be considered as an internally consistent data set for modelling of minority-carrier transport in heavily doped silicon (note: the experimental formula by Slotboom and de Graaff has been determined under the assumption of equal electron mobility in *n*-type and *p*-type silicon). However, the validity of majority-carrier-mobility data (or models) for minority carriers and concomittantly the quoted bandgap-narrowing model may be disputed. We may expect minority- and majority-carrier mobilities to be unequal at high dopant concentrations due to the different scattering mechanisms [46] and the possibly additional effect of minority-carrier trapping in band-tail states [47]. Minority-carrier mobility data have been published by Dziewior and Silber [48] and Burk and De La Torre [49]. The minority-hole mobility, measured in the dopant-concentration range from 10^{17} to 10^{20} cm^{-3}, has been found to differ significantly from the majority-hole mobility. The minority-electron mobility was also found to differ slightly from the majority-electron mobility in the 10^{18} cm^{-3} decade, but unfortunately no reliable data on minority-electron mobility are available in the literature in the dopant-concentration range from 10^{19} to 10^{20} cm^{-3}. To the authors' knowledge neither has a comprehensive, theoretical model been published for minority-carrier mobilities. On the other hand, an independent (theoretical) model for bandgap narrowing has been published by Lee and Fossum [50]. In the authors' view it is, however, incorrect to apply this model in conjunction with majority-carrier-mobility data. We believe that continued research on minority-carrier transport in heavily doped silicon is required for accurate and physically correct modelling. In particular minority-electron mobility data and comprehensive, theoretical models for minority-carrier mobility have to be searched for.

5. CONCLUSIONS

An evaluation of boron diffused pp^+ high–low junctions for BSF purposes, modelled in terms of an effective recombination velocity S_{pp^+}, has been presented. Measured S_{pp^+} values, determined by means of grating-MIS solar-cell analysis, have been related to the physical structure of the high–low junctions using the general approach by Del Alamo *et al.* It has been shown that, by including as much relevant data as are now known concerning the profile of electrically active impurities N_A, Auger and SRH recombination and dopant and field dependent diffusivities and by employing the Slotboom and de Graaff bandgap-narrowing model (degeneracy included), a good agreement is obtained between the measured S_{pp^+} values and the theoretical values. It has also been shown that Auger recombination has a major impact on the minority carrier reflecting capability of the high–low junctions. On the other hand, Shockley–Read–Hall recombination appears to be of minor importance.

Acknowledgements—This paper is part of a report of the Belgian National R-D Program (Prime Ministers Office of Scientific Research, Wetenschapstraat 8, 1040 Brussels, Belgium). R. Girisch has been supported by the European Community.

The authors would like to thank B. Charliers for his assistance with cell fabrication. For the junction profile and junction depth measurements the authors greatly appreciated the help of S. Bakker and K. Visser of the Groningen State University (the Netherlands). Finally one of the authors (R. G.) would like to thank K. De Meyer, H. Maes and L. Deferm for the fruitful discussions.

REFERENCES

1. J. Mandelkorn and J. H. Lamneck, Jr., in *Proc. 9th IEEE Photovoltaic Specialists Conf.* 66–71 (1972).
2. J. Mandelkorn, J. H. Lamneck, Jr. and L. R. Scudder, in *Proc. 10th IEEE Photovoltaic Specialists Conf.* 207–211 (1973).
3. J. R. Hauser and P. M. Dunbar, *IEEE Trans. Electron Dev.* **ED-24**, 305–321 (1977).
4. J. G. Fossum and E. L. Burgess, *Appl. Phys. Lett.* **33**, 238–240 (1978).
5. M. A. Green, R. B. Godfrey and L. W. Davies, in *Proc. 12th IEEE Photovoltaic Specialists Conf.* 896–899 (1976).
6. N. G. Tarr, D. L. Pulfrey and P. A. Iles, *J. Appl. Phys.* **51**, 3926–3929 (1980).
7. N. G. Tarr and D. L. Pulfrey, *Appl. Phys. Lett.* **39**, 83–85 (1981).
8. A. Neugroschel, *IEEE Trans. Electron Dev.* **ED-27**, 287–289 (1980).
9. M. P. Godlewski, C. R. Baraona and H. W. Brandhorst, Jr., in *Proc. 10th IEEE Photovoltaic Specialists Conf.* 40–49 (1973).
10. J. G. Fossum, R. D. Nasby and S. C. Pao, *IEEE Trans. Electron Dev.* **ED-27**, 785–791 (1980).
11. A. Neugroschel, in *Proc. 14th IEEE Photovoltaic Specialists Conf.* 63–71 (1980).
12. R. J. McPartland and A. G. Sabnis, *Solid-St. Electron.* **23**, 605–610 (1980).
13. J. G. Fossum, *IEEE Trans. Electron Dev.* **ED-24**, 322–325 (1977).
14. J. L. Moll and J. M. Ross, *Proc. IRE* **44**, 72–78 (1956).
15. R. P. Mertens, J. F. Nijs, R. J. Van Overstraeten and S. C. Jain, *IEEE Trans. Electron Dev.* **ED-29**, 922–928 (1982).
16. C. T. Chuang, *IEEE Trans. Electron Dev.* **ED-30**, 1709–1716 (1983).
17. P. M. Dunbar and J. R. Hauser, *Solid-St. Electron.* **19**, 95–102 (1976).
18. J. G. Fossum, *Solid-St. Electron.* **19**, 269–277 (1976).
19. J. C. Tandon, D. J. Roulston and S. G. Chamberlain, *Solid-St. Electron.* **15**, 669–685 (1972).
20. A. Sinha and S. K. Chattopadhyaya, *Solid-St. Electron.* **21**, 943–951 (1978).
21. A. Sinha and S. K. Chattopadhyaya, *IEEE Trans. Electron Dev.* **ED-25**, 1412–1414 (1978).
22. J. Del Alamo, J. Eguren and A. Luque, *Solid-St. Electron.* **24**, 415–420 (1981).
23. J. Del Alamo, J. Van Meerbergen, F. D'Hoore and J. Nijs, *Solid-St. Electron.* **24**, 533–538 (1981).
24. J. G. Fossum, R. B. Nasby and E. L. Burgess, in *Proc. 13th IEEE Photovoltaic Specialists Conf.* 1294–1299 (1978).
25. R. Girisch, F. D'Hoore, P. Van Halen, R. Mertens, K. Petit, P. De Pauw and R. Van Overstraeten, in *Proc. 14th IEEE Photovoltaic Specialists Conf.* 1366–1369 (1980).
26. R. Girisch, R. P. Mertens and R. Van Overstraeten, *Solid-St. Electron.* **28**, 1169–1179 (1985).
27. K. D. Rasch, K. Roy, R. Schilling and H. Fischer, in *Proc. 14th IEEE Photovoltaic Specialists Conf.* 141–145 (1980).

28. J. R. Hauser and P. M. Dunbar, *Solid-St. Electron.* **18**, 715–716 (1975).
29. S. R. Dhariwal, R. Gadre and R. K. Mathur, *IEEE Electron Dev. Lett.* **EDL-4**, 105–107 (1983).
30. H. J. J. De Man, *IEEE Trans. Electron Dev.* **ED-18**, 833–834 (1971).
31. R. J. Van Overstraeten, H. J. De Man and R. P. Mertens, *IEEE Trans. Electron Dev.* **ED-20**, 290–298 (1973).
32. A. H. Marshak, M. A. Shibib, J. G. Fossum and F. A. Lindholm, *IEEE Trans. Electron Dev.* **ED-28**, 293–298 (1981).
33. S. Selberherr, A. Schutz and H. Potzl, presented at the Katholieke Universiteit Leuven, Belgium, Summer Course 1983; S. Selberherr, *Microelectron. Reliab.* **24**, 225–257 (1984).
34. J. W. Slotboom and H. C. de Graaff, *Solid-St. Electron.* **19**, 857–862 (1976).
35. D. Kendall, *Conf. Physics and Application of Lithium Diffused Silicon*, NASA-Goddard Space Flight Center, Dec. 1969.
36. I. Lagnado and S. M. Polcari, *Solid-St. Electron.* 1219–1220 (1967).
37. D. A. Antoniadis and R. W. Dutton, *IEEE Trans. Electron Dev.* **ED-26**, 490–500 (1979).
38. W. S. Wang and Y. H. Lo, *IEEE Trans. Electron Dev.* **ED-30**, 1828–1831 (1983).
39. H. Fischer and W. Pschunder, in *Proc. 11th IEEE Photovoltaic Specialists Conf.* 25–31 (1975).
40. J. G. Fossum and D. S. Lee, *Solid-St. Electron.* **25**, 741–747 (1982).
41. H. T. Weaver and R. D. Nasby, *IEEE Trans. Electron Dev.* **ED-28**, 465–472 (1981).
42. J. D. Beck and R. Conradt, *Solid-St. Commun.* **13**, 93–95 (1973).
43. J. Dziewior and W. Schmid, *Appl. Phys. Lett.* **31**, 346–348 (1977).
44. W. Lochmann, *Phys. Stat. Sol. (a)* **45**, 423–432 (1978).
45. R. Girisch, unpublished results.
46. H. S. Bennett, *Solid-St. Electron.* **26**, 1157–1166 (1983).
47. A. Neugroschel and F. A. Lindholm, *Appl. Phys. Lett.* **42**, 176–178 (1983).
48. J. Dziewior and D. Silber, *Appl. Phys. Lett.* **35**, 170–172 (1979).
49. D. E. Burk and V. De La Torre, *IEEE Electron Dev. Lett.* **EDL-5**, 231–233 (1984).
50. D. S. Lee and J. G. Fossum, *IEEE Trans. Electron Dev.* **ED-30**, 626–634 (1983).

APPENDIX 1

In order to avoid an iterative procedure for the solution to the differential equation (8) it is convenient to introduce new variables (see Fig. 6)

$$\left.\begin{aligned} a - x &\equiv \xi \\ N_{A\mathit{eff}}(x) &\rightarrow N^*_{A\mathit{eff}}(\xi) \\ S(x) &\rightarrow S^*(\xi) \end{aligned}\right\}. \tag{A1.1}$$

The differential equation (8) transforms to

$$\frac{\mathrm{d}S^*}{\mathrm{d}\xi} = -\frac{S^{*2}}{D_n} + \frac{S^*}{N^*_{A\mathit{eff}}}\frac{\mathrm{d}N^*_{A\mathit{eff}}}{\mathrm{d}\xi} + \frac{1}{\tau_n} \tag{A1.2}$$

with the boundary condition $S^*(0) = S_B$. The value of $S^*(a) \equiv S_{pp^+}$ is obtained by

$$S_{pp^+} = S_B + \int_0^a \left\{-\frac{S^{*2}}{D_n} + \frac{S^*}{N^*_{A\mathit{eff}}}\frac{\mathrm{d}N^*_{A\mathit{eff}}}{\mathrm{d}\xi} + \frac{1}{\tau_n}\right\}\mathrm{d}\xi. \tag{A1.3}$$

APPENDIX 2

Mobility model

For the concentration and field dependent mobilities we used the formulae presented by Selberherr [33]. The expression for the mobility, which models temperature dependent lattice scattering, scattering at ionized impurities and electron-hole scattering, is in field free silicon given by

$$\mu_{LI}(N,T) = \mu_L(T) \times a + \mu_{min} \times (1 - a) \qquad (\mathrm{cm^2/Vs}) \tag{A2.1}$$

where the mobility, determined by lattice scattering, $\mu_L(T)$ is expressed as

$$\mu_L(T) = A \times T^{-g} \qquad (\mathrm{cm^2/Vs}) \tag{A2.2}$$

and where

$$a = \frac{1}{1 + (T/300)^b \times (N/No)^c}$$

$$N = 0.67 \times (N_D^+ + N_A^-) + 0.33 \times (n + p) \qquad (\mathrm{cm^{-3}}) \tag{A2.3}$$

	A	g	μ_{min}	b	c	N_o
electrons	$7.12\ 10^8$	2.3	55.24	−3.8	0.73	$1.072\ 10^{17}$
holes	$1.35\ 10^8$	2.2	49.7	−3.7	0.7	$1.606\ 10^{17}$

In regions with a high electric field component parallel to the current flow, drift velocity saturation has to be taken into account. This effect has been combined with the previous mechanisms using a Mathiessen-type rule

$$\mu(N,T,E_p) = (\mu_{LI}(N,T)^m + (v_s/E_p)^m)^{1/m} \qquad (\mathrm{cm^2/Vs}) \tag{A2.4}$$

where v_s is the saturation velocity

$$v_s = v_o \times T^h \qquad (\mathrm{cm/s}) \tag{A2.5}$$

	m	v_o	h
electrons	−2	$1.53\ 10^9$	−0.87
holes	−1	$1.62\ 10^8$	−0.52

Bandgap narrowing model and carrier degeneracy

To deduce the effective impurity concentration $N_{A\mathit{eff}}$ from the total electrically active impurity concentration N_A

$$N_{A\mathit{eff}} = N_A \exp(-\Delta E_g(N_A)/V_T) \tag{A2.6}$$

we used the experimentally determined formula for the bandgap narrowing ΔE_g of Slotboom and de Graaff [34]

$$\Delta E_g(N_A) = 9\left\{\ln\frac{N_A}{10^{17}} + \sqrt{\left(\ln^2\frac{N_A}{10^{17}} + 0.5\right)}\right\}\ \mathrm{mV} \qquad \text{(A2.7)}$$

in which the effect of carrier degeneracy is embedded as well.

Lifetime model

The lifetime τ_n was considered to be determined by Shockley–Read–Hall recombination and Auger recombination

$$\tau_n = (\tau_{\mathrm{SRH}}^{-1} + \tau_{\mathrm{Auger}}^{-1})^{-1} \qquad \text{(A2.8)}$$

where the Kendall model [35] was applied for the SRH lifetime τ_{SRH}

$$\tau_{\mathrm{SRH}} = \frac{\tau_o}{1 + \dfrac{N_A}{N_{oA}}} \qquad \text{(A2.9)}$$

and where the Auger lifetime was expressed by

$$\tau_{\mathrm{Auger}} = (C_{ehh}p^2)^{-1}. \qquad \text{(A2.10)}$$

The parameter values used in expressions (A2.9) and (A2.10) are given in Section 3.3.